

AgriFM: A Multi-source Temporal Remote Sensing Foundation Model for Crop Mapping

Wenyuan Li^a, Shunlin Liang^{a,*}, Keyan Chen^b, Yongzhe Chen^a, Han Ma^a, Jianglei Xu^a, Yichuan Ma^a, Shikang Guan^a, Husheng Fang^c, Zhenwei Shi^b

^a*Jockey Club STEM Lab of Quantitative Remote Sensing, Department of Geography, The University of Hong Kong, Hong Kong, China*

^b*Department of Aerospace Intelligent Science and Technology, School of Astronautics, Beihang University, Beijing, China*

^c*School of Remote Sensing and Information Engineering, Wuhan University, China*

Abstract

Escalating climate change and global population growth demand precise crop mapping solutions to ensure food security. Accurate crop mapping fundamentally relies on modeling multi-scale spatiotemporal patterns, where spatial scales range from individual field textures to landscape-level context, and temporal scales capture both short-term phenological transitions and full growing-season dynamics, demanding robust joint spatiotemporal modeling capabilities. Existing approaches are inherently limited by their architectural designs that process spatial and temporal features separately, leading to significant information loss. Transformer-based remote sensing foundation models (RSFMs) offer promising potential for crop mapping due to their innate ability for unified spatiotemporal processing via self-attention mechanisms. However, current RSFMs remain suboptimal for crop mapping: they either employ fixed spatiotemporal windows that ignore the multi-scale nature of crop systems or completely disregard temporal information by focusing solely on spatial patterns. To bridge these gaps, we present AgriFM, a multi-source temporal remote sensing foundation model specifically designed for agricultural crop mapping. Our approach begins by establishing the necessity of simultaneous hierarchical spatiotemporal feature extraction, leading to the development of a modified Video Swin Transformer architecture where temporal down-sampling is synchronized with spatial down-sampling operations. This modified backbone enables efficient unified processing of long time-series satellite inputs while preserving critical multi-scale spatial patterns and phenological dynamics. AgriFM leverages temporally rich data streams from three satellite sources including MODIS, Landsat-8/9 and Sentinel-2, and is pre-trained on a global representative dataset comprising over 25 million image samples supervised by land cover products. The resulting framework incorporates a versatile decoder architecture that dynamically fuses these learned spatiotemporal representations, supporting diverse downstream tasks including cropland mapping, field-boundary delineation, early-season crop mapping, and specific crop mapping (e.g., winter wheat and paddy rice) with different data sources. Comprehensive evaluations demonstrate AgriFM's superior performance over conventional deep learning approaches and state-of-the-art general-purpose RSFMs across all downstream tasks. Notably, AgriFM demonstrates remarkable extensibility by supporting multi-source remote sensing data and variable temporal windows for diverse mapping tasks. Codes will be available at <https://github.com/flyakon/AgriFM> and <https://glass.hku.hk>.

Keywords: Foundation model, crop mapping, remote sensing, deep learning

1. Introduction

The dual challenges of rapid population growth and intensifying climate change impacts have elevated global food security to a pressing priority (Wheeler and Von Braun, 2013; Singh et al., 2023). Satellite remote sensing has become indispensable for addressing this challenge, providing effective tools for large-scale agricultural monitoring and precise crop mapping (Van Tricht et al., 2023; Fang et al., 2024; Chen et al., 2025b). Recent technological advances have enhanced both the spatial and temporal resolution of Earth observation data (Yuan et al., 2020), creating unprecedented opportunities for detailed crop mapping. However, it simultaneously demands more sophisticated analytical methods capable of extracting meaningful agricultural intelligence from complex spatiotemporal patterns.

The growing demands for accurate crop mapping have spurred significant methodological evolution, beginning with phenology-based approaches. They utilize the distinct physical attributes of various crops, including their differing reflectance across spectral bands and their unique phenological traits at various growth phases. Examining and detecting the alterations throughout the crop growth cycle can efficiently differentiate various crops (Qiu et al., 2022; Dong et al., 2020; Qiu et al., 2017; Liang et al., 2024; Ashourloo et al., 2022). Qiu et al. (Qiu et al., 2022) introduced an innovative approach for generating yearly 500-m MODIS-derived national maps of various cropping systems in China, employing phenology-based mapping algorithms and pixel purity thresholds, resulting in an overall accuracy of 89%. Ashourloo et al. (Ashourloo et al., 2022) introduced a novel phenology-based approach utilizing Sentinel-2 time-series data for the efficient differentiation of wheat and barley across extensive regions, attaining an overall accuracy exceeding 76%. The issue with these methods is that they require setting different thresholds based on the mapping task and study area, which significantly affects their applicability. For complex scenarios and tasks, this may lead to erroneous or even failed mapping results.

Machine learning methods (Yin et al., 2020; Yang et al., 2023; Xuan et al., 2023; Van Tricht et al., 2023) have, to a certain extent, resolved the issue of adaptability. They establish the relationship between satellite spectral data and crop types, utilizing algorithms such as Random Forest (Breiman, 2001) and Support Vector Machine (SVM) (Hearst et al., 1998). The effectiveness of machine learning largely depends on obtaining sufficient ground truth data, which is challenging in many scenarios. Van Tricht et al. (Van Tricht et al., 2023) introduced the WorldCereal, a global applicable, seasonally updated crop and irrigation mapping product, which leverages the Random Forest algorithm. He et al. (Yin et al., 2020) developed a novel method based on the Random Forest algorithm to map the extent and timing of abandoned cropland using the Landsat time series and tested this approach in 14 diverse global study regions. Despite the wide application in crop mapping tasks, machine learning methods struggle to simultaneously understand the spatial and temporal information from satellite observations. As a result, they often underperform in complex tasks and lack sufficient processing capacity for large-scale remote sensing data.

*Corresponding author: Shunlin Liang.
Email address: shunlin@hku.hk (Shunlin Liang)

Deep learning, as a subset of machine learning methods, has proven to be a potent tool in processing and understanding big data, propelling significant advancements across diverse fields (Li et al., 2021; Miller et al., 2024; Li et al.). Deep learning models include Convolutional Neural Networks (CNNs) (He et al., 2016), Long Short-Term Memory (LSTM) (Yu et al., 2019), and Transformers (Vaswani et al., 2017). Waldner et al. (Waldner and Diakogiannis, 2020) proposed a data-driven method using ResUNet-a, a deep convolutional neural network with a fully connected UNet backbone, for accurate and scalable extraction of field boundaries from satellite data. As CNNs cannot process temporal remote sensing images, some studies have explored the use of 3D CNNs (Hara et al., 2018) or LSTMs to provide temporal features for these tasks. Gallo et al. (Gallo et al., 2023) proposed an innovative method using 3D Convolutional Neural Networks to process Sentinel-2 time series data, enabling in-season and dynamic crop mapping with real-time updates. Furthermore, some studies have incorporated LSTM to capture additional temporal information, all of which have yielded promising results (Turkoglu et al., 2021; Rußwurm et al., 2023; Barriere et al., 2024).

Recently, transformer models have achieved breakthrough progress in computer vision (Zhang et al., 2024a), remote sensing image processing (Chen et al., 2024), and earth observation tasks (Li et al., 2024). Remote Sensing Foundation Models (RSFMs), built on the basis of transformers, are considered a superior paradigm for handling multi-source temporal remote sensing data (Zhou et al., 2023). Vision Transformer (ViT) (Dosovitskiy et al., 2020) and Swin Transformer (Liu et al., 2021, 2022) are two prominent transformer architectures utilized in the construction of foundation models. RSFMs typically use a large volume of remote sensing data for pre-training, and then a small amount of labeled data for fine-tuning to accomplish specific tasks (Tan et al., 2023; Zhu et al., 2024; Zhou et al., 2024; Lu et al., 2024; Zhang et al., 2024b). The key to pre-training is to help the network learn representations from a large amount of remote sensing data (Cong et al., 2022; Reed et al., 2023). Pre-training methods include masked imaging modeling (MIM) (Hondru et al., 2024) and contrastive learning (CL) (Chen et al., 2020; He et al., 2020; Hondru et al., 2024). In some cases, if a large amount of labeled remote sensing data can be obtained, supervised pre-training is also an effective pre-training method (Feng et al., 2021; Chen et al., 2025a).

Transformer-based RSFMs have demonstrated superior capabilities in extracting spatiotemporal features across various remote sensing tasks, significantly outperforming traditional machine learning methods and deep learning architectures. This suggests RSFMs hold substantial potential for crop mapping, as they can theoretically model complete crop growth cycles end-to-end while integrating multi-source remote sensing data to improve mapping accuracy. Several pioneering studies have begun exploring RSFMs for crop mapping tasks. Fang et al. (Fang et al., 2025) developed a rice mapping method using NASA-IBM's Prithvi foundation model (Jakubik et al., 2023) with Harmonized Landsat and Sentinel-2 (HLS30) data (Claverie et al., 2018) and successfully generated rice distribution maps across Monsoon Asia. Similarly, Qi et al. (Qin et al., 2025) proposed a spatiotemporal masking strategy for pretraining a spatiotemporal collaborative learning network (STCLN) to extract informative representations for crop mapping.

While these approaches demonstrate promising results, they predominantly rely on Vision Transformer (ViT) architectures. This preference stems from ViT's straightforward temporal data processing and relatively lower computational demands during masked image modeling pretraining. However, ViT's inherent downsampling mechanism and fixed spatiotemporal patch windows may adversely affect crop mapping performance. Previous research (Chen et al., 2017; Huang et al., 2020) has proven pixel-wise classification tasks require high spatial feature fidelity, yet ViT's patch embedding operation typically employs aggressive and fixed downsampling (e.g.,

16×16 patches), potentially compromising subtle spatial-temporal differences. Although Fang and Qi's implementations incorporate specialized modifications to mitigate these limitations, such adaptations increase methodological complexity while limiting generalizability.

In contrast, Swin Transformer's hierarchical feature extraction capability - resembling CNN's multi-scale processing - appears better suited for crop mapping tasks. Like U-Net architectures, Swin Transformer can effectively fuse features across scales to enhance spatial precision (Cao et al., 2022). However, existing Swin-based RSFMs remain scarce and typically ignore temporal information, severely limiting their applicability for crop monitoring. While Video Swin Transformer (Liu et al., 2022) inherently supports joint spatiotemporal processing, few existing RSFMs have yet adopted it as the backbone architecture.

To address these gaps, this paper first establishes the necessity of simultaneous hierarchical spatiotemporal feature extraction for crop mapping, leading to the development of a modified Video Swin Transformer (Liu et al., 2022) architecture where temporal down-sampling is synchronized with spatial down-sampling operations. This modified backbone enables efficient unified processing of long time-series satellite inputs while preserving critical multi-scale spatial patterns and phenological dynamics. We then develop AgriFM, a multi-source temporal remote sensing foundation model specifically designed for agricultural crop mapping.

AgriFM leverages temporally rich data streams from MODIS, Landsat-8 / 9, and Sentinel-2 satellites, pre-trained on a global representative dataset with supervision from global land cover products. The pretraining dataset comprises over 25 million globally sampled images from MODIS (250m & 500m), Landsat-8/9 (30m), and Sentinel-2 (10m & 20m). For each satellite source, we randomly selected 16 chronological frames per year to capture complete seasonal variations. Unlike RSFMs relying on MIM or CL for pretraining, we incorporate land cover fraction from GLC_FCS30D data (Zhang et al., 2024c) for supervised pretraining. Specifically, we extract image-level land cover fractions within each sample area as regression targets, optimizing with L1 loss. This approach follows established practices demonstrating land cover priors' effectiveness (Li et al., 2022; Wang et al., 2024). To address inherent label noise in reference products, we implemented an auxiliary teacher network with exponential moving average updates, effectively guiding the model toward robust feature learning while filtering out unreliable supervision signals.

AgriFM incorporates a versatile decoder to dynamically fuse extracted multi-scale spatiotemporal representations, supporting diverse crop mapping tasks, including cropland mapping, field-boundary delineation, early-season crop mapping and specific crop mapping (e.g., winter wheat and paddy rice). For systematic evaluation, we compare AgriFM with three representative approaches: (1) ViT-based temporal RSFMs (Prithvi (Jakubik et al., 2023), SatMAE (Cong et al., 2022)), (2) Swin-based models without temporal processing (PIS (An et al., 2024)), and (3) conventional deep learning methods (CNNs / LSTMs). Experimental results demonstrate AgriFM's consistent superiority, particularly in two crucial aspects: preserving fine-grained spatial details essential for field-level mapping, and effectively modeling long-term temporal patterns critical for crop type analysis - capabilities where existing methods show notable limitations. AgriFM achieves unified processing of heterogeneous data sources, variable temporal sequences, and diverse mapping tasks within a single network architecture. This comprehensive method overcomes the traditional need for task-specific model adaptations while delivering robust performance across various crop mapping tasks.

2. Methodology and Data

In this section, we will delve into the implementation specifics surrounding the AgriFM. The entire flowchart is graphically represented in Figure 1 and can be systematically divided into two primary phases. The first phase involves the creation of a large-scale pre-training dataset and the extraction of land cover fractions to serve as pre-training supervision. The second phase pertains to the development of our multi-source temporal foundation model, along with details of the pre-training process. Based on the foundation mode AgriFM, a unified crop mapping framework is achieved through the construction of a versatile decoder and subsequent fine-tuning with labels.

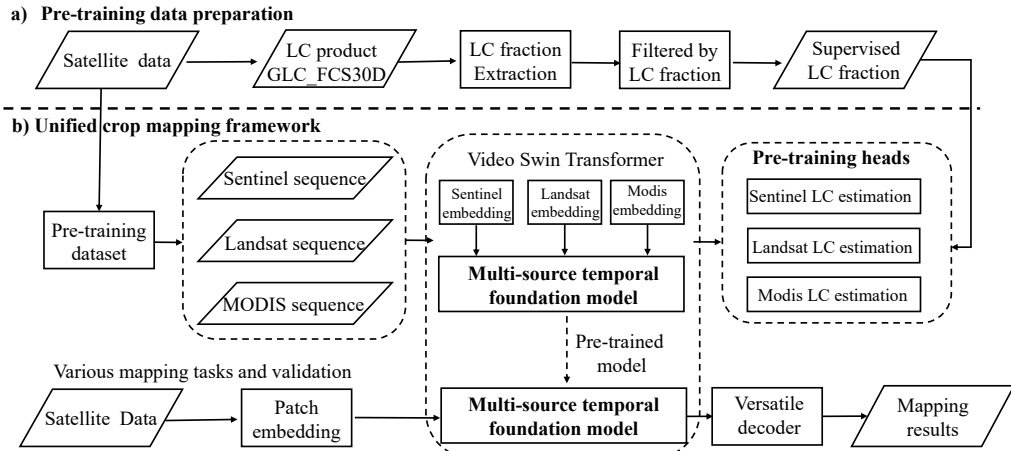


Figure 1: Flowchart outlining the AgriFM: a) The initial phase involves the extraction of pre-training supervision from geographical priors (land cover products) and the assembly of an extensive pre-training dataset, b) The subsequent phase entails the pre-training of the multi-source temporal foundation model and construction of unified crop mapping framework.

2.1. Pre-training Data Preparation

We build a global pre-training dataset composed of multi-source temporal satellite data and land cover fractions from global land cover product GLC_FCS30D (Zhang et al., 2024c).

2.1.1. Multi-source Satellite Data for Pre-training

Satellite data, serving as the input for the foundation models during pre-training, are indiscriminately collected on a global scale from Sentinel-2, Landsat-8/9 and MODIS. The spatial distribution of these pre-training samples is depicted in Figure 2.

The MODIS data from the Terra satellite include the surface reflectance products MOD09A1 and MOD09Q1 with the temporal resolution of 8 days and the spatial resolutions of 500 m and 250 m, respectively. The MOD09Q1 product comprises the first two bands at 250m, and we extract bands 3-7 at 500m from the MOD09A1 product and then re-sample them to 250 meters. The MODIS data selected for pretraining are from 2020 and 2021.

The Landsat surface reflectance data at 30m are extracted from the NASA Harmonized Landsat and Sentinel-2 (HLS) project (Claverie et al., 2018). This is a NASA initiative aimed at creating a harmonized surface reflectance product from the Operational Land Imager (OLI) and

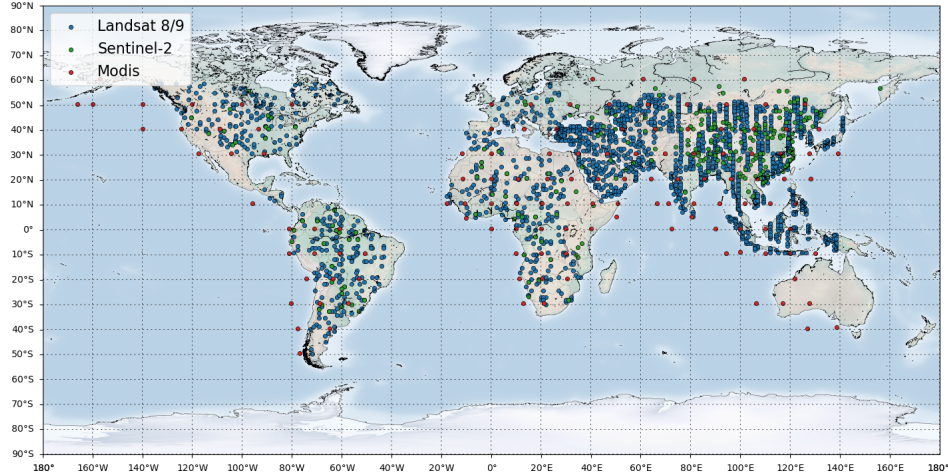


Figure 2: The spatial distribution of pre-training samples collected on a global scale from Sentinel-2, Landsat-8/9 and MODIS.

Multi-Spectral Instrument (MSI) aboard the Landsat-8/9 (L30) and Sentinel-2A/B (S30) remote sensing satellites, respectively. The initiative involves adapting the original projection of Landsat 8/9 to correspond with the projection of Sentinel-2. For the pre-training phase, we globally collect Landsat 8/9 data from HLS L30, with a 30-meter resolution and six bands: Blue, Green, Red, NIR, SWIR 1, and SWIR 2 in 2022. The HLS L30 dataset enhances the native 16-day revisit cycle of individual Landsat satellites to a nominal 4-7 day effective temporal resolution through dual-satellite synergy (Landsat 8/9) and overlapping orbit observations, particularly crucial for capturing rapid crop phenological transitions.

We use the Sentinel-2 data's four bands at 10-m and six bands at 20 m. These bands encompass visible and near-infrared wavelengths, specifically advantageous for differentiating diverse types of vegetation, identifying water bodies, and monitoring urban areas. They include Blue, Green, Red, Red-Edge 1, Red-Edge 2, Red-Edge 3, NIR B08, NIR B08A, SWIR 1, and SWIR 2, and all of them are re-sampled to 10m spatial resolution. All samples are collected in 2021 and 2022, and with a 5-day temporal resolution.

2.1.2. Land Cover Product for Pre-training Supervision

We utilize the GLC_FCS30D (Zhang et al., 2024c) global land cover product for the extraction of land cover fractions for each pre-training sample. These extracted fractions are then used as the pre-training supervision for the foundational model.

GLC_FCS30D is a product of global land cover maps spanning from 1985 to 2022. These maps, which have been generated using Landsat data at a 30m resolution, contain three levels of land cover and a total of 35 finely classified types. The basic classification types we use for pre-training encompass cropland, forest, shrubland, grassland, wetland, water bodies, bare land, and impervious surfaces.

During the pre-training phase, we segment the original satellite data into 224 x 224 sized images. For each image, we determine the land cover distribution within the region it covers, and calculate the fractions accordingly (Li et al., 2021). These land cover fractions will then serve

as pre-training supervision during the pre-training phase. For any input remote sensing image \mathbf{I} , we first extract its geographic coordinate boundaries defined as $\Omega = [x_{min}, x_{max}] \times [y_{min}, y_{max}]$, where x_{min} , x_{max} , y_{min} , and y_{max} represent the minimum longitude, maximum longitude, minimum latitude, and maximum latitude of the image footprint, respectively. From the land cover product \mathcal{L} , we retrieve the corresponding classification map \mathbf{L} within Ω :

$$\mathbf{L} = \mathcal{L}(i, j), \quad \forall (i, j) \in \Omega, \quad (1)$$

where $\mathbf{L}_{i,j} \in 1, 2, \dots, K$ denotes the land cover class at pixel (i, j) , with K being the total number of land covers. In our implementation, we focus on the eight most frequent land covers in the dataset: (1) cropland, (2) forest, (3) shrubland, (4) grassland, (5) wetland, (6) water, (7) bare land, and (8) urban areas. Pixels belonging to other classes are aggregated as background.

The land cover fraction f_k for the k -th land cover class within Ω is computed as:

$$p_k = \frac{1}{N} \sum_{i=1}^H \sum_{j=1}^W \mathbb{I}(L_{ij} = k). \quad (2)$$

$N = H \times W$ is the total number of pixels in Ω . $\mathbb{I}(\dots)$ is the indicator function (1 if true, 0 otherwise). H and W represent the spatial dimensions of the classification map.

The final land cover fraction feature vector is constructed as:

$$\mathbf{p} = [p_0, p_1, p_2, \dots, p_8]^T \in \mathbb{R}^9, \quad (3)$$

where p_0 represents the background land cover and p_1 to p_8 represent the fraction of each land cover.

We employ land cover fractions as supervision instead of the commonly used Masked Image Modeling (MIM) approach for three compelling reasons. First, existing studies (Li et al., 2021) have demonstrated that land cover guidance enables models to acquire valuable geographic priors during pre-training. While the precise mechanistic impact remains challenging to quantify, empirical evidence confirms this constraint significantly improves pre-training efficiency and stability. Methodologically, supervised pre-training aligns with the proven paradigm of early ImageNet pre-training models (Deng et al., 2009), whose effectiveness has been extensively validated. The predominance of MIM largely stems from the scarcity of natural image annotations - a limitation irrelevant to our case, as geo-referenced remote sensing data automatically provides spatially aligned land cover information through geographic coordinates at near-zero annotation cost. This unique advantage allows us to leverage authoritative land cover products while maintaining full scalability.

2.1.3. Pre-training Dataset

After the pre-processing, we have constructed a multi-source temporal remote sensing pre-training dataset, which is derived from MODIS, Landsat 8/9, and Sentinel-2 satellite data at 250m&500m, 30m, and 10m&20m spatial resolution. To meet the input requirements of deep learning models, we randomly select these satellite data and crop the original satellite data into images of 224 x 224 pixels. For each image, a sequence of time series data is also generated with a minimum length of 16. Land cover fractions are computed to serve as pre-training supervision and the image with only background land cover is abandoned.

The pre-training dataset is comprehensively detailed in the Table 1. For each data source, we construct temporal sequences using at least one full year of observations per region. This

Table 1: Detailed information of pre-training dataset. "sequence number" refers to the count of temporal sequences using at least one full year of observations per region, while "total number" indicates the aggregate count of individual images across all sequences.

Source	Resolution	Bands	Sequences number	Images number
MODIS	250m & 500m	7	51964	1574451
Landsat-8/9	30m	6	335985	13392029
Sentinel-2	10m & 20m	10	345843	10277731

ensures that every sample in our dataset captures complete annual vegetation cycles. Specifically, we define three types of temporal sequences corresponding to the model inputs shown in Figure 1: Sentinel-2 sequences, Landsat sequences, and MODIS sequences. Due to computational constraints during pre-training, we randomly sample 16 temporally ordered frames from each annual sequence as model inputs.

In Table 1, "sequence number" refers to the count of temporal sequences using at least one full year of observations per region, while "total number" indicates the aggregate count of individual images across all sequences. The final pre-training dataset comprises 25,244,211 images in total. Notably, we intentionally avoid spatial alignment between different data sources. As illustrated in Figure 1, each pre-training step simultaneously processes temporally and spatially independent Sentinel-2, Landsat, and MODIS sequences from different locations and timestamps. The model estimates land cover fractions separately for each data source, enabling robust cross-sensor feature learning while maintaining computational efficiency.

2.2. Method

In this section, we introduce our proposed multi-source temporal remote sensing foundation model AgriFM for crop mapping. AgriFM is built based on the modified video swin transformer which can accept multi-source temporal remote sensing images as input and extract spatio-temporal features from various downsampling stages. Upon the pre-training of the foundation model, a versatile decoder is formulated. This decoder is capable of accepting features extracted from various stages of downsampling in the foundation model. It is specifically designed to generate a spectrum of crop mapping results, each correlating to its unique set of labels. The overall structure of the framework is shown in Figure 3.

2.2.1. Multi-source Temporal Foundation Model

The input data comprises MODIS data with a resolution of 250m, symbolized as $\mathbf{I}_M \in \mathcal{R}^{7 \times T \times H \times W}$, Landsat data with a resolution of 30m, represented as $\mathbf{I}_L \in \mathcal{R}^{6 \times T \times H \times W}$, and Sentinel-2 data with a resolution of 10m, denoted as $\mathbf{I}_S \in \mathcal{R}^{10 \times T \times H \times W}$. While featuring different numbers of spectral channels (7, 6, and 10 bands respectively), all inputs share identical temporal length and spatial dimensions. To process these multi-source satellite data consistently, we implement separate 3D convolutional patch embedding layers that transform each input modality into a unified embedding representation $\mathbf{E} \in \mathcal{R}^{C_1 \times T_1 \times H_1 \times W_1}$, where $C_1 = 128$ defines the embedding dimension. T_1, H_1 and W_1 are determined by the patch size parameters (S_1, D_1, D_1) in the embedding module, following the relationships $T_1 = \lfloor T/S_1 \rfloor$, $W_1 = \lfloor W/D_1 \rfloor$, and $H_1 = \lfloor H/D_1 \rfloor$. This spatial-temporal patch decomposition allows the model to maintain the structural relationships in the original data while projecting different satellite inputs into a common feature space suitable for subsequent processing.

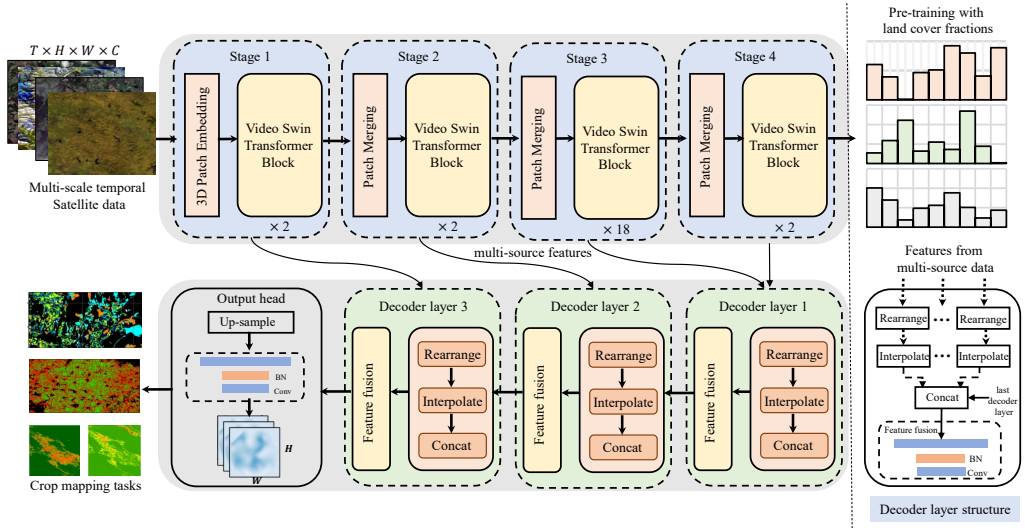


Figure 3: Structure of foundation model, AgriFM, comprising four stages. The input satellite sequences (MODIS, Landsat, and Sentinel-2) are characterized by specific dimensional parameters: T denotes the temporal length of each sequence (set to 16 frames), while W and H represent the spatial width and height (both fixed at 224 pixels). The number of spectral bands, C , varies depending on the data source. The decoder is purposed for the upsampling and fusion of features to yield crop mapping results, each marked by their respective labels.

The embedding representation is then input into the AgriFM, which is constructed based on a modified video swin transformer (Liu et al., 2022). It is proficient at concurrently extracting spatial and temporal features from the input time-series satellite data. The model comprises four hierarchical stages, each containing $2n$ alternating video swin transformer layers: even-numbered layers utilize window-based multi-head self-attention (W-MSA) for local spatiotemporal modeling within non-overlapping $M \times M \times N$ windows, while odd-numbered layers implement shifted window attention (SW-MSA) with shifts along spatial-temporal axes to establish cross-window connections. This dual-attention mechanism effectively balances computational efficiency with global context modeling capabilities.

A key modification from the original architecture is our synchronized spatiotemporal downsampling operation between stages. Unlike conventional approaches that only reduce spatial dimensions, our patch merging module simultaneously compresses both spatial and temporal resolutions through: (1) spatial downsampling via $D_i \times D_i$ patch concatenation and linear projection, and (2) temporal reduction through S_i -frame mean pooling along the time axis. This operation transforms features from stage i as $\mathbf{F}_i \in \mathbb{R}^{T_i \times H_i \times W_i \times C_i}$ to $\mathbf{X}_i \in \mathbb{R}^{T_{i+1} \times H_{i+1} \times W_{i+1} \times C_{i+1}}$, where $T_{i+1} = \lfloor T_i / S_i \rfloor$, $H_{i+1} = \lfloor H_i / D_i \rfloor$, and $W_{i+1} = \lfloor W_i / D_i \rfloor$. The channel dimension expands to $C_{i+1} = 2C_i$ to preserve information capacity. This progressive spatiotemporal abstraction is particularly crucial for agricultural applications, where long input sequences (typically 16-32 temporal observations) must be distilled into single-frame classification outputs while maintaining discriminative crop growth patterns.

2.2.2. Supervised Pre-training with Land Cover Fractions

During the pre-training phase, multi-source temporal satellite data are initially fed into the patch embedding module and backbone networks for feature extraction. The input data comprises MODIS data with a resolution of 250m, symbolized as $\mathbf{I}_M \in \mathcal{R}^{7 \times T \times H \times W}$, Landsat data with a resolution of 30m, represented as $\mathbf{I}_L \in \mathcal{R}^{6 \times T \times H \times W}$, and Sentinel-2 data with a resolution of 10m, denoted as $\mathbf{I}_S \in \mathcal{R}^{10 \times T \times H \times W}$. These input data possess varying input channels, but identical time length and size, where T, H, W are 16, 224, 224, respectively.

As previously introduced, we devise multiple patch embedding modules for each different source of satellite data. The embedding for MODIS, Landsat, and Sentinel are respectively symbolized as $\mathbf{E}_M, \mathbf{E}_L, \mathbf{E}_S$. After embedding, each source of data is transformed into the same dimension, allowing it to be processed by a shared backbone, which is our improved video Swin Transformer. For each patch merging, both temporal and spatial dimensions are downsampled by a factor of two. Subsequently, we use average pooling to convert the output of the final stage, denoted as \mathbf{X}_4 into a vector \mathbf{x} , enabling the estimation of land cover fractions for the input image. We implement a two-layered MLP (multilayer perceptron) network to estimate the land cover fractions \mathbf{p} .

For training objects, we employ the L1 loss function to compute the pre-training losses, utilizing the land cover fractions extracted from GLC_FCS30D as supervision:

$$L_p = \sum_{i=1}^N |\hat{\mathbf{p}}_i - \mathbf{p}_i|, \quad (4)$$

where $\hat{\mathbf{p}}_i$ and \mathbf{p}_i correspond to the estimated fractions and the extracted fractions, respectively.

Furthermore, considering the potential for noise interference in the supervised fractions, we implement the mean-teacher method (Tarvainen and Valpola, 2017; Li et al., 2021) to mitigate the possible impact of noise on foundation model pre-training. We construct a duplicate teacher network, mirroring the structure of the original networks, while referring to the original networks as the student network. During each iteration of pre-training computation, we calculate the fraction as estimated by the teacher network, denoted as \mathbf{q} . We then compute the loss function between this teacher-estimated fraction and the student network's output $\hat{\mathbf{p}}$:

$$L_t = \sum_{i=1}^N |\mathbf{q}_i - \hat{\mathbf{p}}_i|, \quad (5)$$

The parameters of the teacher network are not subjected to updates via gradient descent. Rather, they are updated using a moving average method with a minimal step, derived from the student network:

$$\theta_t = \alpha \cdot \theta_t + (1 - \alpha) \cdot \theta_s, \quad (6)$$

In this equation, θ_t denotes the teacher network parameters, θ_s represents the student network parameters, and α is a decay factor which governs the pace at which the teacher network parameters are updated.

2.2.3. Versatile Decoder for Unified Crop Mapping

The multi-source temporal foundation model enables the unified crop mapping to process heterogeneous temporal remote sensing data from multiple sources, facilitating feature extraction at different sampling stages. While the foundation model provides powerful feature extraction capabilities, it cannot directly generate crop mapping results. To effectively utilize these multi-scale

temporal features, we design a versatile decoder architecture that unifies various crop mapping tasks.

For a given crop mapping task with K input data sources (where K represents any combination of MODIS, Landsat, and Sentinel data), the foundation model first extracts features from each source independently. The decoder reconstructs a single crop map through three upsampling layers, each doubling resolution via upsampling and convolutional layers. Decoder layer j fuses two inputs: 1) upsampled features U_{j-1} from the previous layer (initialized with stage 4 encoder outputs X_4), and 2) skip-connected features X_i from encoder stage $i = 4 - j$. Each decoder layer contains four key operations: rearrange, interpolate, concat, and feature fusion. Given features $\mathbf{F}_i \in \mathbb{R}^{T_i \times H_i \times W_i \times C_i}$ from the i -th stage of the foundation model, the rearrange operation combines the temporal and channel dimensions to produce $\mathbf{F}'_i \in \mathbb{R}^{H_i \times W_i \times (T_i \times C_i)}$. The interpolate function then performs upsampling to match the required spatial dimensions. The concat operation merges the upsampled features with the previous decoder layer's output along the channel dimension, yielding $\mathbf{U}_j^c \in \mathbb{R}^{H_i \times W_i \times (K \times C_i + C_{i-1})}$. Finally, the feature fusion module, implemented with two convolutional layers and a batch normalization layer, processes the concatenated features to generate the decoder layer output \mathbf{U}_j .

For tasks requiring auxiliary data inputs, our framework can directly integrate additional feature maps (e.g., from CNNs) by bypassing the rearrange operation. The final decoder output is processed through a classification layer to produce mapping results. The training objective minimizes the cross-entropy loss:

$$L = - \sum_i y_i \log(p_i) \quad (7)$$

where y_i denotes the ground truth label and p_i represents the predicted probability. To address the prevalent class imbalance in crop mapping tasks, we implement a hard sample mining strategy that focuses learning on challenging examples during training.

2.3. Downstream Crop Mapping Tasks and Validation

Since our goal is to construct the foundation model for crop mapping, our validation emphasis lies in ensuring the optimal performance of our method when labels are available. On one hand, we seek to validate the efficacy of our proposed AgriFM in handling a variety of crop mapping tasks, while on the other hand, we aim to demonstrate that it outperforms the existing remote sensing foundation models. To this end, we have selected five representative crop mapping tasks across three regions for validation, including 1) cropland mapping, 2) crop field boundary delineation 3) early-season crops mapping, 4) paddy field mapping, and 5) winter wheat mapping. The satellite data and other detailed information required for validating these tasks are shown in Table 2. For each task, there are corresponding training, validation, and test sets. The spatial distribution of these data is illustrated in Figure 4.

2.3.1. Cropland Mapping, Field Boundary Delineation, and Early-season Crop Mapping

For the tasks of cropland mapping, crop field boundary delineation, and early-season crop mapping in the Auvergne-Rhône-Alpes (ARA) region of France, we derive labels from the EuroCrops dataset (Schneider et al., 2023). EuroCrops is an all-encompassing dataset featuring geo-referenced polygons of agricultural croplands that cover 16 countries within the European Union (EU). It also provides data on specific crop types cultivated across these regions. This dataset allows us to obtain a comprehensive distribution of crops in the region from 2018 to

2020. Using this information, we generate labels for both cropland areas and boundaries, and select 16 crops as labels for the early-season crop mapping task. We utilize Sentinel-2 data from three consecutive years, 2018, 2019, and 2020, for training, validation, and testing respectively. Similar to the pre-training data processing, we aggregate the 10-meter and 20-meter resolution bands of the Sentinel-2 satellite into a unified 10-meter resolution, resulting in data across 10 spectral bands. For each task, we randomly select 2327 images, each measuring 256×256 pixels.

For cropland mapping and field boundary delineation tasks, we utilize the first 32 available scenes from the first six months of each year as model inputs. In contrast, the early-season crop classification task employs a distinct temporal sampling strategy: we select 4 scenes per month to construct a 24-scene time series. This design serves dual purposes: (1) to explicitly validate our model's capability in handling variable-length temporal inputs, and (2) to incorporate prior knowledge from previous year's cropping patterns. The prior information, extracted using a ResNet50 (He et al., 2016) backbone, is concatenated with the foundation model's output features. To maintain computational efficiency while ensuring feature richness, we deliberately limit the input sequence to 24 frames for this specific task. These experiments are designed to assess the effectiveness of our method in addressing high-resolution crop mapping tasks over extended temporal scales.

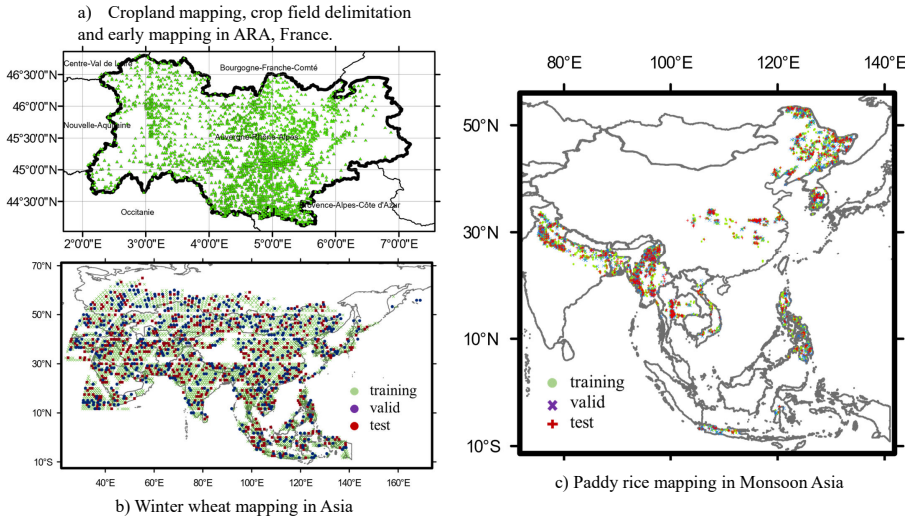


Figure 4: The study area and dataset detailed information for crop mapping tasks.

2.4. Paddy Rice Mapping in Monsoon Asia

For the task of rice mapping, we adopt the method proposed by Fang et al. (Fang et al., 2025) to generate labels from areas of high confidence by comparing and integrating existing products. We select five HLS30 (Harmonized Landsat and Sentinel-2) images from the first six months of 2019, prioritizing those with minimal cloud coverage, to serve as input data. Given that rice is typically cultivated in regions with high cloud coverage, the inclusion of additional temporal data is generally advantageous. Thus, we enrich our dataset with MODIS data, which boasts a higher temporal resolution. Both data sources, despite their differing resolutions, are effectively

Table 2: Detailed information on crop mapping tasks and datasets.

Tasks	Region	Split	Year	Sources	Resolution	Bands	Sequences length	Images Number	Images size
Cropland Mapping Field Boundary delineation	ARA, France	training	2018	Sentinel-2	10m	10	32	2327	256
	ARA, France	validation	2019	Sentinel-2	10m	10	32	2327	256
	ARA, France	testing	2020	Sentinel-2	10m	10	32	2327	256
Early-season Crop Mapping	ARA, France	training	2018	Sentinel-2	10m	10	24	2327	256
	ARA, France	validation	2019	Sentinel-2	10m	10	24	2327	256
	ARA, France	testing	2020	Sentinel-2	10m	10	24	2327	256
Paddy Rice Mapping	Monsoon Asia	training	2019	HLS30 & MODIS	30m & 250m	6&7	5&46	3039	224&56
	Monsoon Asia	validation	2019	HLS30 & MODIS	30m & 250m	6&7	5&46	1013	224&56
	Monsoon Asia	testing	2019	HLS30 & MODIS	30m & 250m	6&7	5&46	1013	224&56
Winter Wheat Mapping	Asia	training	2021	MODIS	250m	7	11	2711	512
	Asia	validation	2021	MODIS	250m	7	11	636	512
	Asia	testing	2021	MODIS	250m	7	11	569	512

harnessed for rice mapping. This task is designed to evaluate the efficacy of our method in rice mapping and demonstrate how our proposed method can effectively leverage the benefits of integrating multiple data sources.

Specifically, the rice mapping tasks are conducted in the Monsoon Asia region, utilizing 2019 data for training, validation, and testing. The input data are sourced from both HLS30 and MODIS, with respective resolutions of 30m and 250m, and providing 6 and 7 spectral bands. The sequence length for the HLS30 and MODIS data is 5 and 46, respectively. In total, 3039 images are used for training, while 1013 images are used for both validation and testing. The image sizes for the HLS30 and MODIS data are 224 and 56, respectively.

2.5. Winter Wheat Mapping in Asia

For the task of winter wheat mapping, we follow the method proposed by Li et al. (Li et al.) to generate labels for winter wheat in Asia based on the WorldCereal product (Van Tricht et al., 2023). In accordance with the growth cycle of winter wheat in Asia, we select one MODIS image per month from August 2020 to June 2021 to form the training input sequence. Specifically, the winter wheat mapping tasks are carried out in Asia, using MODIS data for training, validation, and testing. The input data are derived from MODIS with a resolution of 250m, providing 7 spectral bands. The sequence length for the MODIS data is 11. In total, 2711 images are used for training, 636 images for validation, and 569 images for testing. The image size for the MODIS data is 512.

We use precision (P), recall (R), F1 score (F1), and Overall Accuracy (OA) as our validation metrics:

$$\begin{aligned}
 P &= \frac{TP}{TP + FP}, \\
 R &= \frac{TP}{TP + FN}, \\
 F1 &= 2 \cdot \frac{P \cdot R}{P + R}, \\
 OA &= \frac{TP + TN}{TP + FP + TN + FN},
 \end{aligned} \tag{8}$$

where TP, FP, TN, FN represent the number of true positive samples, false positive samples, true negative samples and false negative samples.

To comprehensively evaluate AgriFM’s performance, we conduct comparisons across three distinct methodological categories. First, we examine conventional deep learning architectures widely adopted in crop mapping: (1) A CNN (VGG16 variant (Simonyan and Zisserman, 2014)) treating temporal observations as additional input channels; (2) A CNN-LSTM hybrid extracting spatial features per timestep using VGG16 followed by temporal modeling through LSTM; and (3) A 3D CNN processing spatiotemporal cubes (height \times width \times time \times bands). All baselines employ identical decoder structures and training protocols to isolate architectural differences, ensuring fair comparison of their spatiotemporal representation capabilities.

Second, we compare against ViT-based foundation models that incorporate temporal information during pretraining. Specifically, we evaluate SatMAE (Cong et al., 2022) (using Landsat-8 data) and Prithvi (Jakubik et al., 2023) (trained on HLS30 data), which represent the most temporally-aware open-source RSFMs currently available, despite their limited sequence lengths. These comparisons reveal how feature fusion strategies and hierarchical representations impact mapping precision, particularly for crops with subtle spectral-temporal signatures.

Third, we analyze PIS, a Swin Transformer-based foundation model lacking explicit temporal processing. While sharing similar backbone architecture and pretraining data scales with our approach, PIS’s non-temporal design helps isolate the benefits of our temporal-aware pretraining strategy. Although PIS uses the Swin transformer as its backbone, we can reuse some weights as pre-trained weights of the video Swin transformer and adopt the same architecture as our method for comparison.

2.6. Implementation details

We develop our codes using Python 3.11 and PyTorch-2.0. During the pre-training phase, the network learning rate is set to 1e-5. To ensure the stability of pre-training, the learning rate gradually increases from 1e-7 to 1e-5 over the first 5000 iterations, after which it gradually decreases throughout the pre-training process until it reaches 1e-6. The pre-training phase lasts for 50 epochs. The training is carried out on ten L40 GPUs, with a batch size of 80. The coefficient for the moving average is set to 0.001.

For downstream crop mapping tasks, we employ the same network structure, that is, the unified crop mapping framework that we construct. The learning rate is set to 6e-5. All experiments are conducted on four L40 GPUs, with a batch size of 16, and last for 50 epochs. We select the model that performs best on the validation dataset as our final result.

3. Cropland Mapping and Field Boundary Delineation

This experiment evaluates the AgriFM’s performance for cropland mapping and field boundary delineation with time series Sentinel-2 images. Utilizing three consecutive years (2018-2020) of Sentinel-2 data over France’s Auvergne-Rhône-Alpes (ARA) region, we process 10 spectral bands aggregated to 10m resolution, with 32 temporal steps per annual sequence. The dataset comprises 2,327 geo-referenced tiles (256 \times 256 pixels) per year, strictly partitioned by temporal years: 2018 for training, 2019 for validation, and 2020 for testing. Boundary delineation presents distinct challenges from cropland mapping, requiring precise field edge detection that demands higher spatial granularity (d’Andrimont et al., 2023; Persello et al., 2023).

As detailed in Tables 3 and 4, we systematically evaluate three methodological categories: (1) CNN variants (CNN, CNN-LSTM, 3DCNN) representing conventional deep learning approaches; (2) ViT-based methods (SatMAE, Prithvi) as current mainstream remote sensing foundation models pretrained with temporal data; and (3) Swin transformer (PIS, AgriFM-scratch)

Table 3: Performance comparison on cropland mapping task (%). Positive class metrics focus on cropland identification.

Model	Positive (Cropland)			Average			
	Precision	Recall	F1	Precision	Recall	F1	OA
CNN	73.30	71.71	73.00	75.03	75.00	75.01	75.18
CNN-LSTM	79.74	81.06	80.39	81.63	81.70	81.66	81.75
3DCNN	80.30	75.70	77.93	80.22	79.89	80.00	80.21
SatMAE (ViT-L)	76.85	76.76	76.80	78.47	78.47	78.47	78.60
Prithvi (ViT-b)	74.66	72.73	73.69	75.90	75.79	75.83	76.02
PIS (Swin-b)	80.11	77.94	79.01	80.81	80.67	80.73	80.88
AgriFM-scratch	79.53	78.47	79.00	80.64	80.58	80.60	80.74
AgriFM	79.35	84.63	81.90	82.68	82.87	82.70	82.74

Table 4: Performance comparison on field boundary delineation task (%). Metrics computed at field boundary pixels.

Model	Positive (Boundary)			Average			
	Precision	Recall	F1	Precision	Recall	F1	OA
CNN	67.20	67.90	67.55	73.84	73.93	73.88	75.42
CNN-LSTM	73.53	70.92	72.20	78.16	77.74	77.94	79.43
3DCNN	68.85	66.98	67.90	74.61	74.33	74.46	76.14
SatMAE (ViT-L)	59.13	66.28	62.50	68.57	69.29	68.78	70.04
Prithvi (ViT-b)	52.81	54.10	53.45	62.32	62.44	62.38	64.50
PIS (Swin-b)	70.44	71.98	71.20	76.64	76.86	76.70	78.07
AgriFM-scratch	70.63	73.70	72.13	77.15	77.59	77.35	78.55
AgriFM	73.93	73.63	73.78	79.02	78.97	78.99	80.29

demonstrating hierarchical feature extraction’s impact on crop mapping. Notably, PIS’s backbone is Swin transformer and doesn’t adopt temporal data. We adaptively rearrange its partial parameters to initialize our Video Swin Transformer, enabling comparison of temporal-agnostic pretraining effects. AgriFM-scratch serves as the randomly initialized control. The “Positive” column specifies cropland / boundary-specific metrics, while “Average” incorporates background class performance. Figure 5 visually contrasts core metrics (Precision / Recall / F1) across methods, and Figure 7 showcases actual mapping outputs where green denotes cropland and red indicates boundaries.

For cropland mapping (Table 3), CNN architectures demonstrate strong baseline performance, with CNN-LSTM leading at 80.39% F1-score due to its explicit spatiotemporal fusion design. 3DCNN achieves only 77.93% F1 despite 3D convolutions. This shows that simply adding 3D convolution does not guarantee better spatiotemporal modeling, and also shows that the 3D convolution in traditional deep learning methods for processing spatiotemporal data may have insufficient information extraction capabilities for crop mapping tasks. ViT-based SatMAE and Prithvi trail significantly at 76.80% and 73.69% F1 respectively, confirming ViT’s architectural constraints—the 16×16 patch embedding causes irreversible spatial detail loss (evident in Figure 7’s blurred boundaries). While increasing input resolution could theoretically mitigate this issue, the computational cost becomes prohibitive for temporal sequences while distorting original resolution relationships. The Swin-based PIS achieves 79.01% F1, outperforming all ViT variants and underscoring hierarchical features’ importance, despite its non-temporal pretraining.

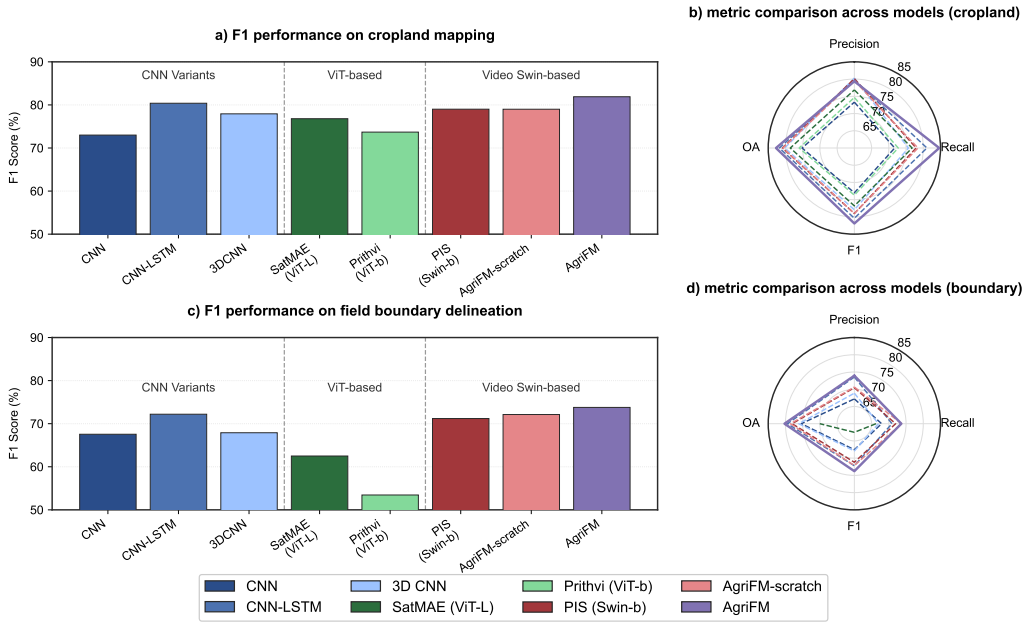


Figure 5: Comparative performance on cropland mapping and boundary delineation task. Bar plots show F1-score for the positive class across models, grouped by architecture type (CNN variants, ViT-based, and Video Swin-based). Radar plots show metrics (precision, recall, F1-score and OA) comparison across models.

AgriFM dominates with 81.90% F1 (84.63% recall), affirming both Video Swin’s architectural superiority for crop mapping and the added value of temporal-aware pretraining.

Boundary delineation (Table 4) further accentuates methodological differences. ViT performance plummets (SatMAE: 62.50% F1; Prithvi: 53.45% F1), consistent with Figure 6’s oversmoothed edges—ViT’s aggressive downsampling struggles with sub-pixel boundary variations. CNN-LSTM maintains relative robustness (72.20% F1). PIS shows architectural promise (71.20% F1) but trails AgriFM by 2.58%, primarily due to lacking temporal pretraining. Intriguingly, randomly initialized Swin-scratch achieves 72.13% F1, merely 1.65% below AgriFM, suggesting hierarchical backbone inherently excels at spatial sensitivity while temporal pretraining provides systematic refinement. The underperformance of PIS versus Agri-scratch highlights incompatibilities when rearranging non-temporal pretrained weights, justifying our dedicated spatiotemporal pretraining strategy.

Three principal conclusions emerge from above experiments and analysis: (1) ViT’s aggressive downsampling fundamentally limits agricultural applications requiring fine spatial outputs; (2) Video Swin transformer’s hierarchical design shows superior potential when combined with temporal pretraining; (3) AgriFM synergizes architectural and pretraining innovations to deliver both global spatiotemporal understanding and pixel-level precision.

We utilize our trained AgriFM to generate a map of cropland and its boundaries in the ARA region of France for the year 2020, as illustrated in Figure 7. The green areas represent cropland, while the red areas delineate the boundaries of this cropland.

As indicated in the generated maps, our proposed model AgriFM demonstrates high effectiveness in mapping cropland and delineating its boundaries. However, it is worth noting that in

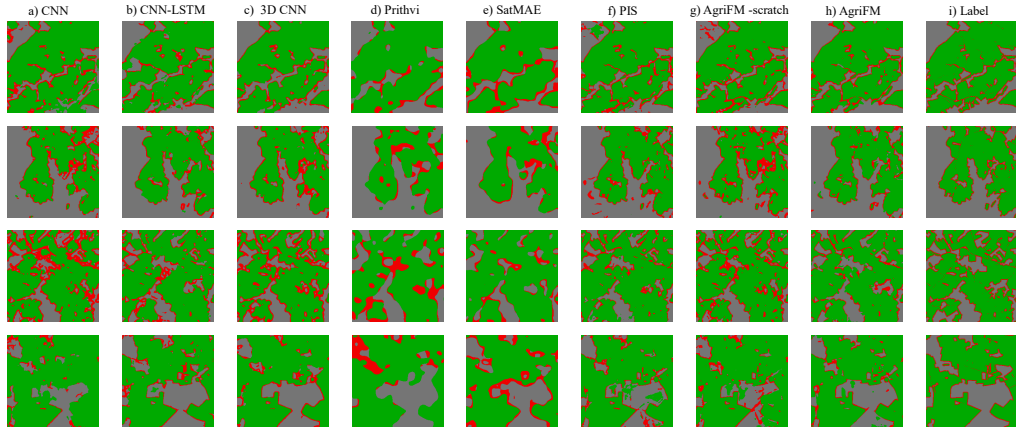


Figure 6: Visual comparison of cropland mapping and field boundary delineation results (green: cropland pixels, red: delineated boundaries) demonstrating method-specific spatial characteristics.

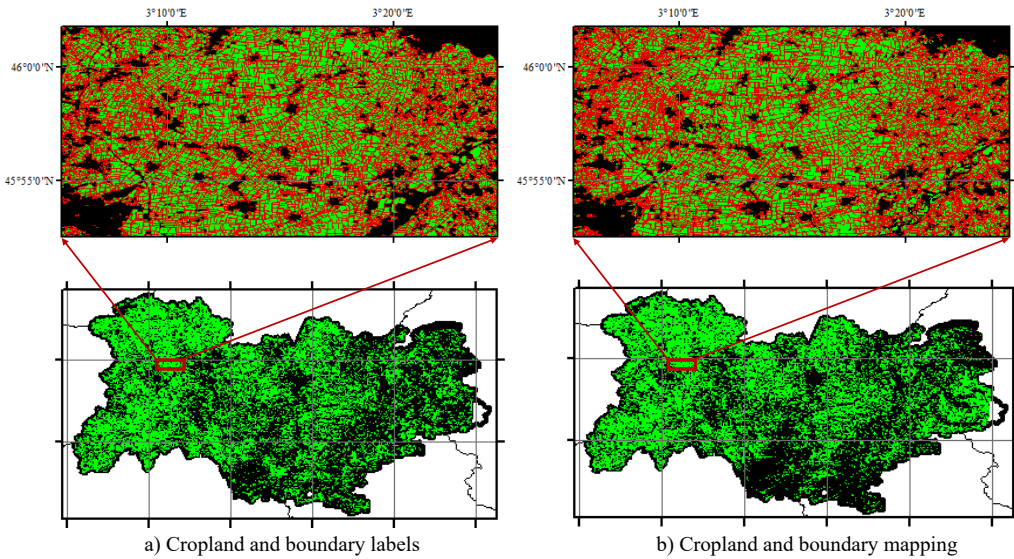


Figure 7: The generated map of cropland and its boundaries in the ARA region of France for the year 2020: a) labels from EuroCrops dataset; b) the mapping results from our method. The green areas represent cropland, while the red areas delineate the boundaries of this cropland.

Table 5: Performance comparison on early-season crop mapping (%).

Model	Precision	Recall	F1-score	OA
CNN	43.50	36.71	40.12	73.04
CNN-LSTM	52.47	40.23	44.29	74.74
3DCNN	46.57	36.81	40.60	73.71
SatMAE (ViT-L)	64.80	40.24	46.10	71.03
Prithvi (ViT-b)	60.00	37.16	42.10	68.68
PIS (Swin-b)	67.11	48.63	54.51	76.18
Swin-scratch	70.43	48.35	54.82	76.26
AgriFM	68.63	53.88	59.88	77.51

areas where cropland is less dense, instances of under-detection may occur. Furthermore, while the method excels at defining boundaries within the cropland, the discontinuity at the borders of the cropland presents a challenge. This is an inherent limitation of the approach we have employed, as the paradigm rooted in semantic segmentation cannot ensure the continuity of the segmentation results.

4. Early-season Crop Mapping

This experiment specifically assesses the model’s capability to recognize crop types during early growth stages—a critical requirement for proactive agricultural management. Leveraging the same Sentinel-2 dataset (10m resolution, 10 spectral bands) and spatial coverage (ARA region, France) as the cropland mapping task, we specifically target classification of 16 major crops during their initial six-month growth phases using 2018-2020 data. The temporal sequence construction adopts a stratified sampling approach: four observations per month are selected, generating 24 temporal observations that capture early phenological development. The 2,327 tiles per year maintain strict temporal isolation: 2018 (training), 2019 (validation), and 2020 (testing).

As shown in Table 5, we systematically compare various methods on 16-crop early-season crop mapping using four metrics: precision, recall, F1-score, and overall accuracy (OA). Figure 8 presents three complementary visualizations: (a) bar charts comparing F1 scores, (b) radar plots showing metric balance, and (c) line graphs analyzing F1-scores across crops ordered by training sample frequency (low to high). Figure 9 further displays spatial mapping comparisons in representative regions.

The results demonstrate AgriFM’s clear superiority with 59.88% F1 and 77.51% OA. Architecturally similar approaches (PIS: 54.51% F1; AgriFM-scratch: 54.82% F1) also significantly outperform alternatives. Notably, the performance gaps between CNN/ViT methods and AgriFM (13-15% F1) are markedly larger than in previous cropland mapping tasks, underscoring the heightened challenge of early-season classification requiring precise spatiotemporal feature coordination. Three key observations emerge: (1) CNN variants (best: CNN-LSTM 44.29% F1) excel at spatial feature fusion but lack temporal modeling capacity; (2) ViT-based methods (best: SatMAE 46.10% F1) leverage global attention for temporal modeling but sacrifice spatial detail; (3) AgriFM uniquely integrates both capabilities through multi-source temporal modeling and pretraining.

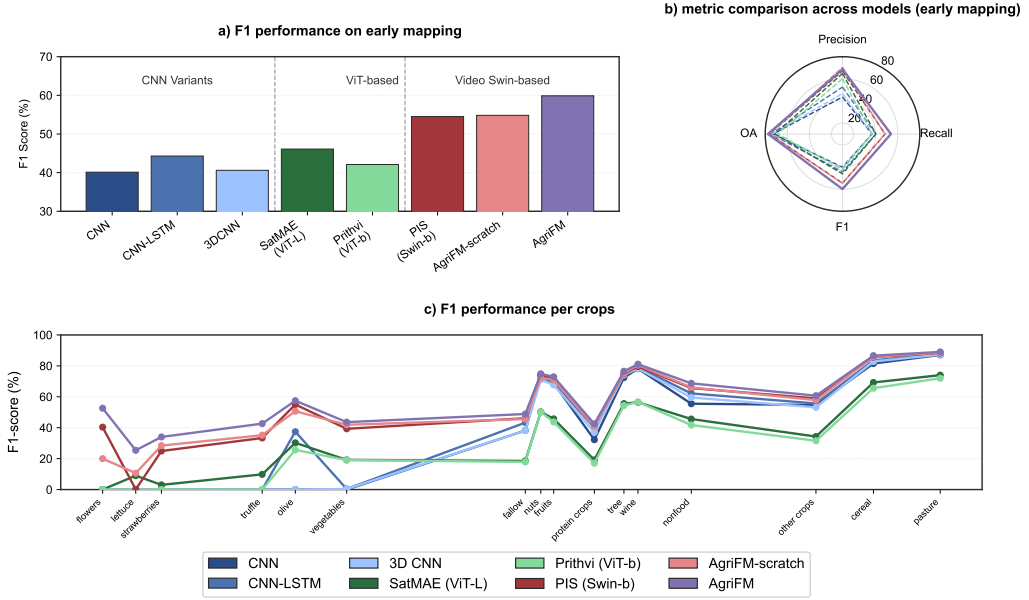


Figure 8: Early-season crop type mapping analysis: (a) Method-wise metric comparison, (b) Balanced performance radar chart, (c) Per-class F1 scores ordered by training sample frequency.

Figure 8 c) reveals distinct response patterns to class imbalance. ViT-based methods show advantages for rare crops (left side), benefiting from global temporal context capture. Conversely, CNNs outperform ViTs for dominant crops (right side), where local spatial features prove more discriminative. AgriFM maintains remarkably stable performance across all frequency categories, achieving high F1 improvement for rare crops versus suboptimal methods.

Spatial results in Figure 9 exhibit three characteristic patterns: (1) CNN variants preserve field boundaries but suffer misclassification; (2) ViT methods show superior class discrimination but blurred boundaries and small-field omissions; (3) AgriFM achieves both accurate crop identification and sharp boundary delineation. These findings collectively validate that hierarchical temporal modeling synergistically optimizes classification accuracy and spatial precision.

Three principal conclusions emerge from the above analysis: First, early-season crop classification demands delicate balance between temporal and spatial feature extraction that conventional single-advantage architectures cannot provide. Second, multi-source temporal pretraining effectively mitigates class imbalance challenges. Third, AgriFM's unified design delivers optimal performance across all scenarios, establishing a new paradigm for precision agriculture. These insights provide both theoretical and practical guidance for agricultural remote sensing model development.

We also employ our trained AgriFM to generate a map of the early crop distribution in the ARA region of France for the year 2020, as depicted in Figure 10. Our model leverages satellite data from the first half of the year, ensuring an accurate mapping of crop distribution in the first half of each year. The map produced by our method effectively reflects the actual crop planting scenario for that year. As can be observed from the figure, there is a high level of crop diversity within the same area, yet our method successfully differentiates between different crops.

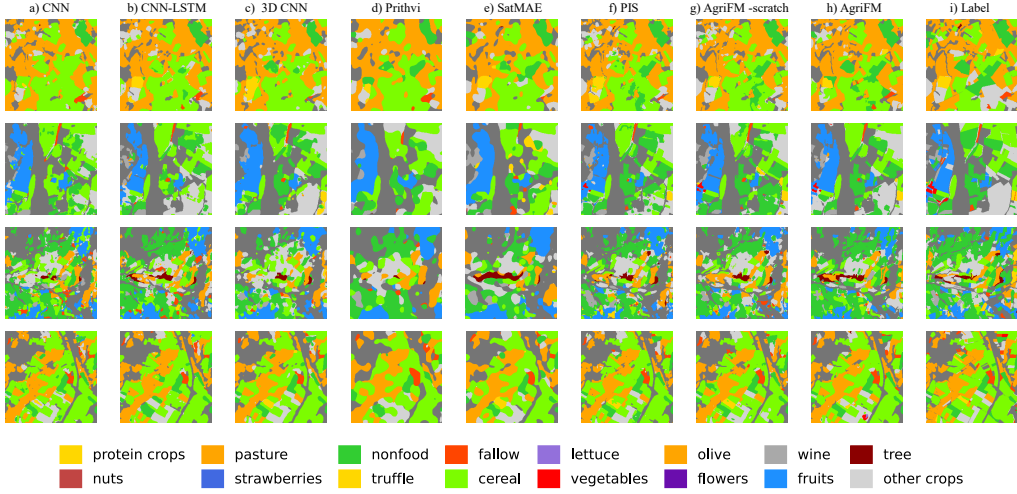


Figure 9: Visual comparison of early-season crop mapping results.

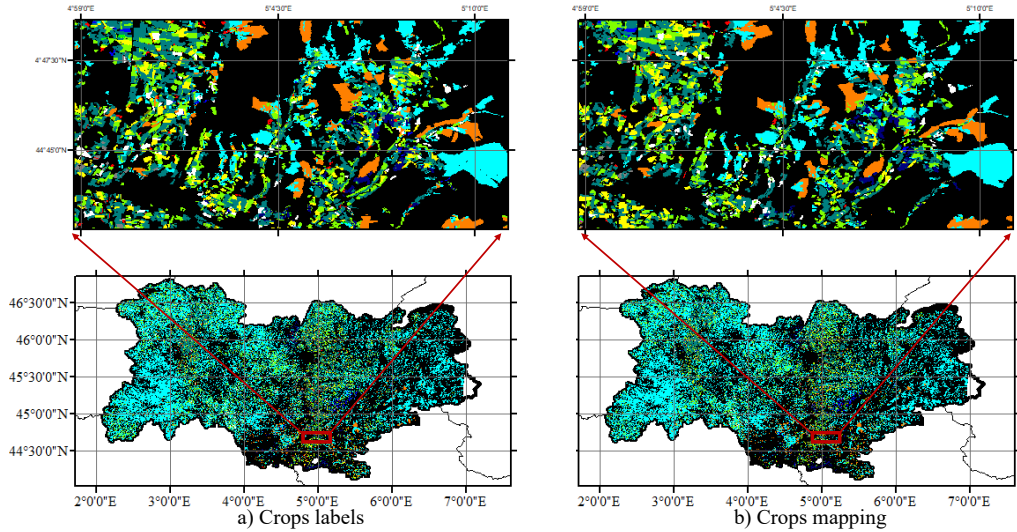


Figure 10: Generated map of early-season crops in the ARA region of France for the year 2020: a) labels from EuroCrops dataset; b) the mapping results from our method.

Table 6: Comparison results on paddy rice mapping in Monsoon Asia with different methods.

Model	Source	Positive (Rice)			Average			
		Precision	Recall	F1	Precision	Recall	F1	OA
CNN	HLS30	82.61	89.35	85.85	89.04	90.82	89.85	91.43
CNN-LSTM	HLS30	81.87	88.62	85.11	88.52	90.28	89.32	90.97
3DCNN	HLS30	81.48	88.38	84.79	88.27	90.07	89.08	90.77
SatMAE (ViT-L)	HLS30	80.72	85.88	83.22	87.39	88.73	88.01	89.92
Prithvi (ViT-b)	HLS30	79.45	86.10	82.64	86.77	88.48	87.54	89.47
PIS (Swin-b)	HLS30	83.46	89.75	86.49	89.56	91.22	90.32	91.84
AgriFM-scratch	HLS30	80.84	90.17	85.25	88.30	90.70	89.35	90.92
AgriFM	HLS30	83.30	88.98	86.04	89.32	90.82	90.02	91.60
	HLS & MODIS	83.74	90.85	87.15	89.92	91.80	90.78	92.20

5. Paddy Rice Mapping in Monsoon Asia

This experiment evaluates the AgriFM’s capacity to synergize multi-resolution satellite data for paddy rice mapping in Asia. We fuse Harmonized Landsat-Sentinel (HLS30) imagery (30m spatial resolution, 6 spectral bands, 5 temporal steps) with MODIS observations (250m&500m resolution, 7 bands, 44 temporal steps) across Monsoon Asia’s rice cultivation belt during 2019. A total of 3,039 training samples 1013 validation samples and 1013 test samples are drawn from high-confidence rice parcels identified through consensus of existing products. Input sequences span the critical rice-growing period (January-June).

The experimental results in Table 6 demonstrate the comparative performance of different methods for paddy rice mapping across monsoon Asia using HLS30 data. All models are tested under consistent conditions, with AgriFM evaluated in two configurations: HLS30-only input and combined HLS30-MODIS input. Figure 11 shows some representative rice mapping results.

Swin-based methods consistently outperform other architectures, with PIS achieving 86.49% F1 and 90.32% average F1. This 3-4% advantage over CNN variants (best: CNN at 85.85% F1) and 4-5% over ViT models (best: SatMAE at 83.22% F1) confirms the superiority of hierarchical feature extraction for rice mapping. Notably, the randomly initialized Swin-scratch shows competitive performance (85.25% F1), suggesting the inherent suitability of Swin’s architecture for agricultural patterns.

Considering the frequent cloud cover in the Monsoon Asia region, we incorporate MODIS data to aid in rice mapping. The experimental results suggest that the inclusion of MODIS data can enhance recall from 88.98% to 90.85%. This indicates that a larger proportion of rice can be correctly identified, emphasizing the effectiveness of our approach in extracting and integrating features from the MODIS input with those derived from HLS30. However, it can be observed that the precision decreases slightly with the inclusion of MODIS data. Although the F1 score still improves, the increase is not substantial. This is likely due to the significant difference in resolution between MODIS and HLS30. Furthermore, the accuracy of rice mapping using only HLS30 is already quite high, implying that in most scenarios, the best results can be achieved using only HLS30. Nevertheless, these findings still demonstrate that our proposed method can effectively integrate and process multi-source remote sensing data.

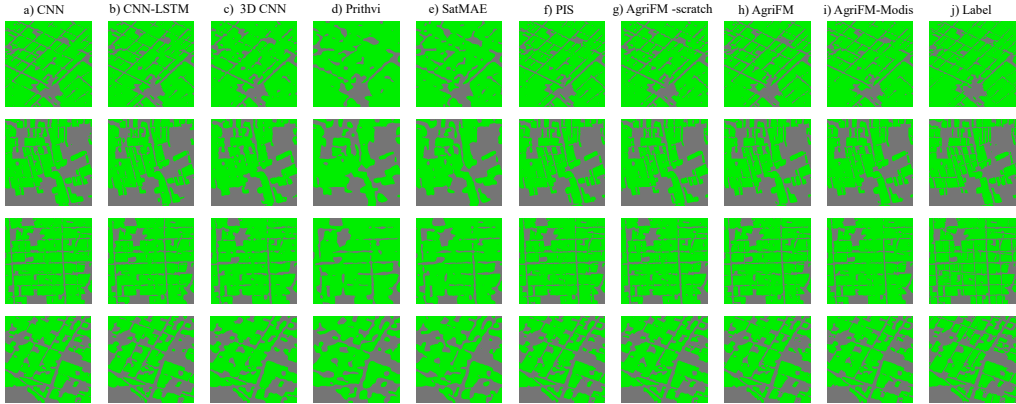


Figure 11: Visual comparison of paddy rice mapping in Monsoon Asia.

6. Winter Wheat Mapping in Asia

This experiment validates the AgriFM’s performance on Asia’s winter wheat mapping. we process MODIS monthly composites (250m&500m spatial resolution, 7 spectral bands) spanning 11 critical growth stages from pre-sowing (August 2020) to harvest (June 2021). The dataset comprises 2,711 training, 636 validation, and 569 testing tiles (512×512 pixels), geographically stratified to represent diverse agroclimatic zones from the North China Plain to Central Asian steppes.

Table 7 presents a comprehensive evaluation of winter wheat mapping across Asia using low-resolution satellite data. Figure 12 shows some representative visualization for winter wheat mapping. AgriFM achieves state-of-the-art performance with 75.40% wheat F1-score and 97.11% overall accuracy (OA), outperforming Prithvi (66.61% F1, 95.96% OA) and SatMAE (67.17% F1, 96.23% OA) by significant margins.

Several key observations emerge from the comparative analysis. First, Swin-based methods consistently dominate the rankings, with PIS (74.47% F1) and Swin-scratch (74.23% F1) already surpassing all CNN and ViT variants. This 6-8% F1 advantage over ViT models particularly highlights the importance of hierarchical feature extraction when working with low-resolution inputs. Notably, the standard CNN achieves better performance (70.17% F1) than more complex 3DCNN (67.69% F1) and CNN-LSTM (68.27% F1) architectures, suggesting that simple spatial feature extractors may be more effective than sophisticated spatiotemporal designs for this specific task.

The superior performance of AgriFM can be attributed to two synergistic factors. First, its MODIS-specific pretraining captures unique phenological patterns critical for winter wheat identification - an advantage missing in other models. Second, the architecture’s multi-source design enables exceptional feature extraction from low-resolution data, evidenced by its best-in-class recall (78.74%), indicating superior detection of true wheat areas. This combination proves especially valuable for winter wheat mapping, where the crop’s distinct growth stages create temporally identifiable signatures in MODIS data.

In addition, while winter wheat’s strong phenological characteristics make it relatively distinguishable from other crops, the performance gaps between methods are larger than those observed in rice mapping (Table 6). This accentuates our model’s specialized capabilities - the

Table 7: Comparison results on winter wheat mapping in Asia with different methods.

Model	Positive (Winter wheat)			Average			
	Precision	Recall	F1	Precision	Recall	F1	OA
CNN	73.10	67.46	70.17	85.59	82.99	84.23	96.77
CNN-LSTM	66.53	70.11	68.27	82.37	84.00	83.16	96.34
3DCNN	64.53	71.17	67.69	81.40	84.42	82.83	96.18
SatMAE (ViT-L)	65.76	68.64	67.17	81.94	83.26	82.58	96.23
Prithvi (ViT-b)	62.20	71.70	66.61	80.25	84.55	82.23	95.96
PIS (Swin-b)	73.17	75.82	74.47	85.86	87.07	86.46	97.08
Agri-scratch	71.78	76.85	74.23	85.20	87.52	86.32	97.00
AgriFM	72.34	78.74	75.40	85.53	88.47	86.93	97.11

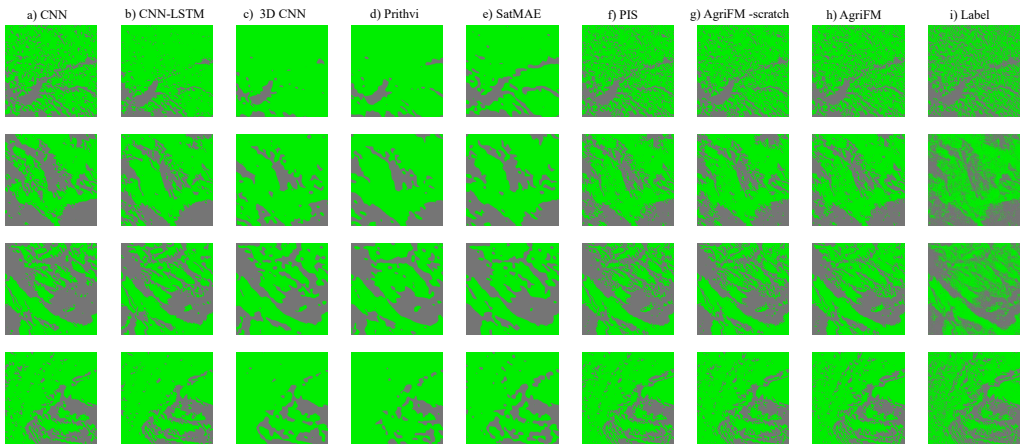


Figure 12: Visual comparison of winter wheat mapping in Asia.

8.8% F1 improvement over ViT models and 5.2% over CNNs demonstrate AgriFM’s particular aptitude for leveraging subtle temporal cues in coarse-resolution data.

7. Discussions

To further validate the robustness and versatility of our proposed framework, we conduct more systematic analyses addressing critical operational aspects of crop mapping tasks: temporal adaptability, and data efficiency. These experiments are designed as follows.

- Quantify the model’s capacity to handle variable-length temporal sequences—a fundamental requirement for crop mapping across diverse phenological cycles and cloud cover conditions. We systematically evaluate its performance on early-season crop mapping using temporally downsampled input sequences. Specifically, we down-sample the original Sentinel-2 time series into fixed-interval sequences of 8-, 12-, and 16-step configurations. This simulates scenarios with varying observational frequencies while preserving phenological relevance.

Table 8: Evaluation of the model’s capacity to handle variable-length temporal sequences (8-, 12-, 16-, and 24-step sequences).

Sequence length	Precision	Recall	F1	OA
8-step sequences	69.05	45.63	50.50	74.55
12-step sequences	70.07	48.72	54.87	76.14
16-step sequences	70.50	50.07	56.45	76.23
24-step sequences	68.63	53.88	59.88	77.43

Table 9: Evaluate practical applicability under constrained label availability scenarios (10%, 20%, 33%, 50% subsets).

Training subsets	Model	Precision	Recall	F1	OA
10%	wo/ pre-training	53.21	33.87	38.28	71.45
	w/ pre-training	59.31	32.56	37.65	70.67
20%	wo/ pre-training	57.11	41.36	46.77	74.28
	w/ pre-training	64.36	42.07	48.11	73.92
33%	wo/ pre-training	65.54	45.04	50.43	75.31
	w/ pre-training	62.10	48.09	52.85	75.57
50%	wo/ pre-training	65.40	47.75	54.06	75.70
	w/ pre-training	65.42	52.17	57.63	76.26
100%	wo/ pre-training	70.43	48.35	54.82	76.20
	w/ pre-training	68.63	53.88	59.88	77.43

- Evaluate practical applicability under constrained label availability scenarios (10%, 20%, 33%, 50% subsets). Critically, we compare against non-pretrained variants of our framework (random initialization) to quantify the benefits of foundation model pretraining. This demonstrates the value of large-scale self-supervised learning in label-scarce agricultural settings.

As evidenced by Table 8, the framework demonstrates progressive performance gains with extended temporal sequences, attaining an F1 score of 59.88% and overall accuracy (OA) of 77.43% for 24-step sequences. A critical observation is the pronounced improvement in recall, which rises from 45.63% (8-step) to 53.88% (24-step)—a 17.5% relative increase—indicating enhanced discrimination of crop-specific phenological patterns as temporal contexts expand. This aligns with our line chart visualizations from Figure 13 a), where recall exhibits a near-linear correlation with sequence length, suggesting that longer time series better resolve phenological ambiguities. Notably, even under sparse 8-step inputs, the model retains 84.3% (50.50 vs. 59.88) of its peak F1 performance, underscoring its effectiveness in leveraging both spectral-spatial patterns and partial phenological cues. Interestingly, while precision peaks at 70.50% for 16-step sequences before slightly declining, OA consistently improves (+3.88% from 8- to 24-step). These results validate the framework’s dual capacity: preserving spatial fidelity under temporal sparsity while capitalizing on extended sequences to capture growth-stage dynamics.

The label efficiency analysis (Table 9 and Figure 13 b)) underscores the practical value of our foundation model pretraining strategy. As the fine-tuning dataset scales from 10% to 100%,

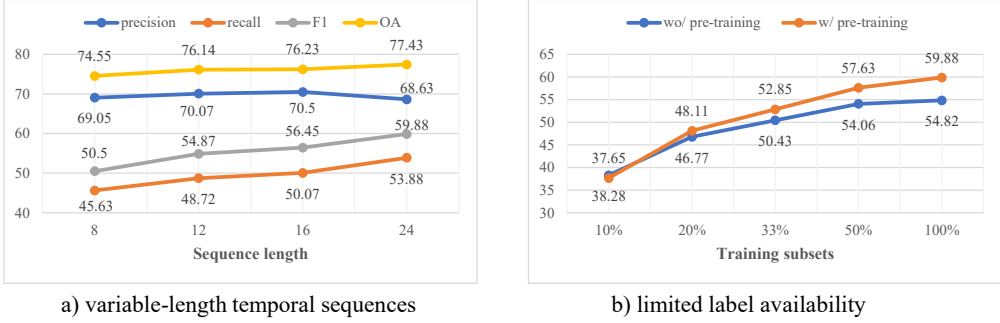


Figure 13: Systematic analyses addressing critical operational aspects of crop mapping tasks: temporal adaptability and data efficiency.

the pretrained variant demonstrates consistent performance gains, achieving a 57.63% F1 score with only 50% fine-tuning data—surpassing the non-pretrained model’s full-data performance (54.82%). This highlights the pretraining framework’s ability to extract transferable spatiotemporal representations, enabling effective adaptation to downstream tasks with limited annotations. Notably, while the non-pretrained model plateaus beyond 50% fine-tuning data ($\Delta F1=+0.76\%$ from 50% to 100%), the pretrained variant continues to improve ($\Delta F1=+2.25\%$), suggesting superior utilization of additional labeled samples.

At the 10% fine-tuning level, the pre-trained model exhibits a precision-recall imbalance (59.31% precision vs. 32.56% recall), with recall nearly matching the non-pretrained counterpart (32.56% vs. 33.87%). This phenomenon likely stems from insufficient fine-tuning data to fully adapt the pretrained features for distinguishing subtle inter-class variations, causing the model to prioritize precision over recall. However, as fine-tuning data increases to 20%, the pre-trained model establishes a decisive advantage (+1.34% F1), demonstrating its capacity to leverage pretrained knowledge for improved generalization. Notably, the pretrained model achieves comparable performance to its non-pretrained counterpart using significantly less data: at just 33% fine-tuning data (F1=52.85%), it matches the non-pretrained model’s full-data performance (F1=54.82%). This demonstrates the strong transferability of pretrained representations, enabling effective deployment in regions with limited labeled data.

8. Conclusion

This paper first addresses and validates the necessity of simultaneous hierarchical spatiotemporal feature extraction for crop mapping. It leads to the development of a modified Video Swin Transformer architecture where temporal down-sampling is synchronized with spatial down-sampling operations. Capitalizing on this finding, we introduce AgriFM, a multi-source temporal remote sensing foundation model with specialized spatiotemporal modeling for agricultural crop mapping. AgriFM integrates multi-source satellite data including MODIS, Landsat-8/9, and Sentinel-2, and employs geographical prior land cover products for supervised pre-training. It effectively addresses the limitations of existing RSFMs, ensuring the incorporation of multi-resolution data, providing comprehensive coverage of the crop growth cycle, optimizing the use of geographical information, and offering a unified framework for a wide array of crop mapping

tasks. These tasks include, but are not limited to, cropland mapping, cropland boundary delineation, early-season crop mapping, and specific tasks like winter wheat and rice mapping. The effectiveness and adaptability of AgriFM have been substantiated through superior performance across a variety of crop mapping tasks, demonstrating its potential as an immediately applicable solution for leveraging deep learning in more precise and efficient crop mapping.

The significance of this method lies not only in its immediate practical application but also in its potential for future advancements in this critical field. With the escalating global population growth and climate change, food security has become a pressing issue requiring efficient crop mapping, and satellite remote sensing plays a pivotal role in this regard. However, the challenges presented by current methods necessitate the development of more efficient and precise models such as AgriFM. By addressing the limitations of existing RSFMs and providing a comprehensive framework for diverse tasks, AgriFM paves the way for future advancements in crop mapping, contributing significantly to the efforts towards achieving global food security.

Despite the agricultural applications, the natural extension of this work lies in assessing the model’s generalizability to other Earth observation tasks. Many geo-spatial applications similarly require simultaneous processing of spatiotemporal data, suggesting our foundation model could serve as a versatile backbone. However, task-specific adaptations—particularly in decoder design—remain necessary. For vegetation parameter estimation (e.g., LAI and FVC), for instance, the decoder must generate time-specific outputs rather than integrated predictions. While Swin Transformer outperforms other architectures for crop mapping, performance variations across tasks are substantial. For certain image classification or regression tasks, ViT-based methods may still prevail due to their global representation capabilities.

Our results confirm that pretraining significantly boosts performance, especially for complex tasks. However, architectural suitability remains equally crucial. This study’s practical implication is clear: for crop mapping tasks, Video Swin Transformer should be the architecture of first consideration, with domain-specific pretraining then applied for additional gains. This two-stage approach—selecting the optimal architecture followed by targeted pretraining—proves more effective than relying solely on either component.

Regarding pretraining strategies, while masked image modeling and contrastive learning dominate current practice, our choice of land cover supervision offers distinct advantages. Existing studies have demonstrated the value of incorporating remote sensing-specific knowledge into pretraining. As a fundamental geographic prior, land cover information provides rich semantic guidance. This raises intriguing possibilities—many other Earth observation products (e.g., biomass, soil moisture) could theoretically serve as pretraining supervision, though their effectiveness requires systematic evaluation.

Data Availability

Codes will be available on the website of the Jockey Club STEM Lab of Quantitative Remote Sensing, HKU (<https://glass.hku.hk>) and <https://github.com/flyakon/AgriFM>.

Acknowledgment

The research work described in this paper was conducted in the JC STEM Lab of Quantitative Remote Sensing funded by The Hong Kong Jockey Club Charities Trust.

The computations were performed using research computing facilities offered by Information Technology Services, the University of Hong Kong.

References

- An, X., He, W., Zou, J., Yang, G., Zhang, H.. Pretrain a remote sensing foundation model by promoting intra-instance similarity. *IEEE Transactions on Geoscience and Remote Sensing* 2024;.
- Ashourloo, D., Nematollahi, H., Huete, A., Aghighi, H., Azadbakht, M., Shahrabi, H.S., Goodarzdashti, S.. A new phenology-based method for mapping wheat and barley using time-series of sentinel-2 images. *Remote Sensing of Environment* 2022;280:113206.
- Barriere, V., Claverie, M., Schneider, M., Lemoine, G., d'Andrimont, R.. Boosting crop classification by hierarchically fusing satellite, rotational, and contextual data. *Remote Sensing of Environment* 2024;305:114110.
- Breiman, L.. Random forests. *Machine learning* 2001;45:5–32.
- Cao, H., Wang, Y., Chen, J., Jiang, D., Zhang, X., Tian, Q., Wang, M.. Swin-unet: Unet-like pure transformer for medical image segmentation. In: *European conference on computer vision*. Springer; 2022. p. 205–218.
- Chen, K., Liu, C., Chen, B., Li, W., Zou, Z., Shi, Z.. Dynamicvis: An efficient and general visual foundation model for remote sensing image understanding. *arXiv preprint arXiv:250316426* 2025a;.
- Chen, K., Liu, C., Chen, H., Zhang, H., Li, W., Zou, Z., Shi, Z.. Rsprompter: Learning to prompt for remote sensing instance segmentation based on visual foundation model. *IEEE Transactions on Geoscience and Remote Sensing* 2024;.
- Chen, L.C., Papandreou, G., Kokkinos, I., Murphy, K., Yuille, A.L.. Deeplab: Semantic image segmentation with deep convolutional nets, atrous convolution, and fully connected crfs. *IEEE transactions on pattern analysis and machine intelligence* 2017;40(4):834–848.
- Chen, T., Kornblith, S., Norouzi, M., Hinton, G.. A simple framework for contrastive learning of visual representations. In: *International conference on machine learning*. PMLR; 2020. p. 1597–1607.
- Chen, Y., Liang, S., Li, W., Fang, H., Ma, H., Xu, J., Ma, Y., Guan, S., Zhang, F.. The first algorithm for mapping high-resolution cropland inundation status throughout the growing season using swot karin data. Available at SSRN 5090896 2025b;.
- Claverie, M., Ju, J., Masek, J.G., Dungan, J.L., Vermote, E.F., Roger, J.C., Skakun, S.V., Justice, C.. The harmonized landsat and sentinel-2 surface reflectance data set. *Remote sensing of environment* 2018;219:145–161.
- Cong, Y., Khanna, S., Meng, C., Liu, P., Rozi, E., He, Y., Burke, M., Lobell, D., Ermon, S.. Satmae: Pre-training transformers for temporal and multi-spectral satellite imagery. *Advances in Neural Information Processing Systems* 2022;35:197–211.
- d'Andrimont, R., Claverie, M., Kempeneers, P., Muraro, D., Yordanov, M., Peressutti, D., Batić, M., Waldner, F.. Ai4boundaries: an open ai-ready dataset to map field boundaries with sentinel-2 and aerial photography. *Earth System Science Data* 2023;15(1):317–329.
- Deng, J., Dong, W., Socher, R., Li, L.J., Li, K., Fei-Fei, L.. Imagenet: A large-scale hierarchical image database. In: *2009 IEEE conference on computer vision and pattern recognition*. Ieee; 2009. p. 248–255.
- Dong, J., Fu, Y., Wang, J., Tian, H., Fu, S., Niu, Z., Han, W., Zheng, Y., Huang, J., Yuan, W.. Early-season mapping of winter wheat in china based on landsat and sentinel images. *Earth System Science Data* 2020;12(4):3081–3095.
- Dosovitskiy, A., Beyer, L., Kolesnikov, A., Weissenborn, D., Zhai, X., Unterthiner, T., Dehghani, M., Minderer, M., Heigold, G., Gelly, S., et al. An image is worth 16x16 words: Transformers for image recognition at scale. *arXiv preprint arXiv:201011929* 2020;.
- Fang, H., Liang, S., Chen, Y., Ma, H., Li, W., He, T., Tian, F., Zhang, F.. A comprehensive review of rice mapping from satellite data: Algorithms, product characteristics and consistency assessment. *Science of Remote Sensing* 2024;100172.
- Fang, H., Liang, S., Li, W., Chen, Y., Ma, H., Xu, J., Ma, Y., He, T., Tian, F., Zhang, F., et al. Generating an annual 30m rice cover product for monsoon asia (2018–2023) using harmonized landsat and sentinel-2 data and the nasa-ibm geospatial foundation model. Available at SSRN 5138538 2025;.
- Feng, Y., Jiang, J., Tang, M., Jin, R., Gao, Y.. Rethinking supervised pre-training for better downstream transferring. *arXiv preprint arXiv:211006014* 2021;.
- Gallo, I., Ranghetti, L., Landro, N., La Grassa, R., Boschetti, M.. In-season and dynamic crop mapping using 3d convolution neural networks and sentinel-2 time series. *ISPRS Journal of Photogrammetry and Remote Sensing* 2023;195:335–352.
- Hara, K., Kataoka, H., Satoh, Y.. Can spatiotemporal 3d cnns retrace the history of 2d cnns and imagenet? In: *Proceedings of the IEEE conference on Computer Vision and Pattern Recognition*. 2018. p. 6546–6555.
- He, K., Fan, H., Wu, Y., Xie, S., Girshick, R.. Momentum contrast for unsupervised visual representation learning. In: *Proceedings of the IEEE/CVF conference on computer vision and pattern recognition*. 2020. p. 9729–9738.
- He, K., Zhang, X., Ren, S., Sun, J.. Deep residual learning for image recognition. In: *Proceedings of the IEEE conference on computer vision and pattern recognition*. 2016. p. 770–778.
- Hearst, M.A., Dumais, S.T., Osuna, E., Platt, J., Scholkopf, B.. Support vector machines. *IEEE Intelligent Systems and their applications* 1998;13(4):18–28.

- Hondru, V., Croitoru, F.A., Minaee, S., Ionescu, R.T., Sebe, N.. Masked image modeling: A survey. arXiv preprint arXiv:240806687 2024;.
- Huang, H., Lin, L., Tong, R., Hu, H., Zhang, Q., Iwamoto, Y., Han, X., Chen, Y.W., Wu, J.. Unet 3+: A full-scale connected unet for medical image segmentation. In: ICASSP 2020-2020 IEEE international conference on acoustics, speech and signal processing (ICASSP). IEEE; 2020. p. 1055–1059.
- Jakubik, J., Roy, S., Phillips, C.E., Fraccaro, P., Godwin, D., Zadrozy, B., Szwarcman, D., Gomes, C., Nyirjesy, G., Edwards, B., Kimura, D., Simumba, N., Chu, L., Mukkavilli, S.K., Lambhate, D., Das, K., Bangalore, R., Oliveira, D., Muszynski, M., Ankur, K., Ramasubramanian, M., Gurung, I., Khallaghi, S., Li, H.S., Cecil, M., Ahmadi, M., Kordi, F., Alemohammad, H., Maskay, M., Ganti, R., Weldeniam, K., Ramachandran, R.. Foundation Models for Generalist Geospatial Artificial Intelligence. Preprint Available on arxiv:231018660 2023;.
- Li, W., Chen, K., Chen, H., Shi, Z.. Geographical knowledge-driven representation learning for remote sensing images. IEEE Transactions on Geoscience and Remote Sensing 2021;60:1–16.
- Li, W., Chen, K., Shi, Z.. Geographical supervision correction for remote sensing representation learning. IEEE Transactions on Geoscience and Remote Sensing 2022;60:1–20.
- Li, W., Liang, S., Chen, Y., Ma, H., Xu, J., Chen, Z., Fang, H., Zhang, F.. Asiawheat: The first asian 250-m annual fractional wheat cover time series (2001-2023) using convolutional neural networks and transformer models. Available at SSRN 5029097 ;.
- Li, W., Liu, Z., Chen, K., Chen, H., Liang, S., Zou, Z., Shi, Z.. Deepphysinet: Bridging deep learning and atmospheric physics for accurate and continuous weather modeling. arXiv preprint arXiv:240104125 2024;.
- Liang, S., Chen, Y., Liu, J., Ma, H., Li, W., Sucharitakul, P., Luo, N., Chen, Z., Fang, H., Zhang, F., et al. Mapping paddy rice cropping intensity and calendar in monsoon asia at 20 m resolution between 2018 and 2021 from multi-source satellite data using a sample-free algorithm. Available at SSRN 4948283 2024;.
- Liu, Z., Lin, Y., Cao, Y., Hu, H., Wei, Y., Zhang, Z., Lin, S., Guo, B.. Swin transformer: Hierarchical vision transformer using shifted windows. In: Proceedings of the IEEE/CVF international conference on computer vision. 2021. p. 10012–10022.
- Liu, Z., Ning, J., Cao, Y., Wei, Y., Zhang, Z., Lin, S., Hu, H.. Video swin transformer. In: Proceedings of the IEEE/CVF conference on computer vision and pattern recognition. 2022. p. 3202–3211.
- Lu, S., Guo, J., Zimmer-Dauphinee, J.R., Nieuwsma, J.M., Wang, X., VanValkenburgh, P., Wernke, S.A., Huo, Y.. Ai foundation models in remote sensing: A survey. arXiv preprint arXiv:240803464 2024;.
- Miller, L., Pelletier, C., Webb, G.I.. Deep learning for satellite image time-series analysis: A review. IEEE Geoscience and Remote Sensing Magazine 2024;.
- Persello, C., Grift, J., Fan, X., Paris, C., Hänsch, R., Koeva, M., Nelson, A.. Ai4smallfarms: A dataset for crop field delineation in southeast asian smallholder farms. IEEE Geoscience and Remote Sensing Letters 2023;20:1–5.
- Qin, X., Guo, H., Su, X., Zhao, Z., Wang, D., Zhang, L.. Spatiotemporal masked pre-training for advancing crop mapping on satellite image time series with limited labels. International Journal of Applied Earth Observation and Geoinformation 2025;137:104426.
- Qiu, B., Hu, X., Chen, C., Tang, Z., Yang, P., Zhu, X., Yan, C., Jian, Z.. Maps of cropping patterns in china during 2015–2021. Scientific data 2022;9(1):479.
- Qiu, B., Luo, Y., Tang, Z., Chen, C., Lu, D., Huang, H., Chen, Y., Chen, N., Xu, W.. Winter wheat mapping combining variations before and after estimated heading dates. ISPRS journal of photogrammetry and remote sensing 2017;123:35–46.
- Reed, C.J., Gupta, R., Li, S., Brockman, S., Funk, C., Clipp, B., Keutzer, K., Candido, S., Uyttendaele, M., Darrell, T.. Scale-mae: A scale-aware masked autoencoder for multiscale geospatial representation learning. In: Proceedings of the IEEE/CVF International Conference on Computer Vision. 2023. p. 4088–4099.
- Rußwurm, M., Courty, N., Emonet, R., Lefèvre, S., Tuia, D., Tavenard, R.. End-to-end learned early classification of time series for in-season crop type mapping. ISPRS Journal of Photogrammetry and Remote Sensing 2023;196:445–456.
- Schneider, M., Schelte, T., Schmitz, F., Körner, M.. Eurocrops: The largest harmonized open crop dataset across the european union. Scientific Data 2023;10(1):612.
- Simonyan, K., Zisserman, A.. Very deep convolutional networks for large-scale image recognition. arXiv preprint arXiv:14091556 2014;.
- Singh, B.K., Delgado-Baquerizo, M., Egidio, E., Guirado, E., Leach, J.E., Liu, H., Trivedi, P.. Climate change impacts on plant pathogens, food security and paths forward. Nature Reviews Microbiology 2023;21(10):640–656.
- Tan, C., Cao, Q., Li, Y., Zhang, J., Yang, X., Zhao, H., Wu, Z., Liu, Z., Yang, H., Wu, N., et al. On the promises and challenges of multimodal foundation models for geographical, environmental, agricultural, and urban planning applications. arXiv preprint arXiv:231217016 2023;.
- Tarvainen, A., Valpola, H.. Mean teachers are better role models: Weight-averaged consistency targets improve semi-supervised deep learning results. Advances in neural information processing systems 2017;30.
- Turkoglu, M.O., D'Aronco, S., Perich, G., Liebisch, F., Streit, C., Schindler, K., Wegner, J.D.. Crop map-

- ping from image time series: Deep learning with multi-scale label hierarchies. *Remote Sensing of Environment* 2021;264:112603.
- Van Tricht, K., Degerickx, J., Gilliams, S., Zanaga, D., Battude, M., Grosu, A., Brombacher, J., Lesiv, M., Bayas, J.C.L., Karanam, S., et al. Worldcereal: a dynamic open-source system for global-scale, seasonal, and reproducible crop and irrigation mapping. *Earth System Science Data* 2023;15(12):5491–5515.
- Vaswani, A., Shazeer, N., Parmar, N., Uszkoreit, J., Jones, L., Gomez, A.N., Kaiser, Ł., Polosukhin, I.. Attention is all you need. *Advances in neural information processing systems* 2017;30.
- Waldner, F., Diakogiannis, F.I.. Deep learning on edge: Extracting field boundaries from satellite images with a convolutional neural network. *Remote sensing of environment* 2020;245:111741.
- Wang, Y., Albrecht, C.M., Zhu, X.X.. Multi-label guided soft contrastive learning for efficient earth observation pretraining. *arXiv preprint arXiv:240520462* 2024;.
- Wheeler, T., Von Braun, J.. Climate change impacts on global food security. *Science* 2013;341(6145):508–513.
- Xuan, F., Dong, Y., Li, J., Li, X., Su, W., Huang, X., Huang, J., Xie, Z., Li, Z., Liu, H., et al. Mapping crop type in northeast china during 2013–2021 using automatic sampling and tile-based image classification. *International Journal of Applied Earth Observation and Geoinformation* 2023;117:103178.
- Yang, G., Li, X., Liu, P., Yao, X., Zhu, Y., Cao, W., Cheng, T.. Automated in-season mapping of winter wheat in china with training data generation and model transfer. *ISPRS Journal of Photogrammetry and Remote Sensing* 2023;202:422–438.
- Yin, H., Brandão Jr, A., Buchner, J., Helmers, D., Iuliano, B.G., Kimambo, N.E., Lewińska, K.E., Razenkova, E., Rizayeva, A., Rogova, N., et al. Monitoring cropland abandonment with landsat time series. *Remote Sensing of Environment* 2020;246:111873.
- Yu, Y., Si, X., Hu, C., Zhang, J.. A review of recurrent neural networks: Lstm cells and network architectures. *Neural computation* 2019;31(7):1235–1270.
- Yuan, Q., Shen, H., Li, T., Li, Z., Li, S., Jiang, Y., Xu, H., Tan, W., Yang, Q., Wang, J., et al. Deep learning in environmental remote sensing: Achievements and challenges. *Remote sensing of Environment* 2020;241:111716.
- Zhang, J., Huang, J., Jin, S., Lu, S.. Vision-language models for vision tasks: A survey. *IEEE Transactions on Pattern Analysis and Machine Intelligence* 2024a;.
- Zhang, M., Yang, B., Hu, X., Gong, J., Zhang, Z.. Foundation model for generalist remote sensing intelligence: potentials and prospects. *Science Bulletin* 2024b;.
- Zhang, X., Zhao, T., Xu, H., Liu, W., Wang, J., Chen, X., Liu, L.. Glc_fcs30d: the first global 30 m land-cover dynamics monitoring product with a fine classification system for the period from 1985 to 2022 generated using dense-time-series landsat imagery and the continuous change-detection method. *Earth System Science Data* 2024c;16(3):1353–1381.
- Zhou, C., Li, Q., Li, C., Yu, J., Liu, Y., Wang, G., Zhang, K., Ji, C., Yan, Q., He, L., et al. A comprehensive survey on pretrained foundation models: A history from bert to chatgpt. *arXiv preprint arXiv:230209419* 2023;.
- Zhou, Y., Feng, L., Ke, Y., Jiang, X., Yan, J., Yang, X., Zhang, W.. Towards vision-language geo-foundation model: A survey. *arXiv preprint arXiv:240609385* 2024;.
- Zhu, X.X., Xiong, Z., Wang, Y., Stewart, A.J., Heidler, K., Wang, Y., Yuan, Z., Dujardin, T., Xu, Q., Shi, Y.. On the foundations of earth and climate foundation models. *arXiv preprint arXiv:240504285* 2024;.